Microstructural and Chemical Constitution of the Oxide Scale formed on a Pesting-Resistant Mo-Si-Ti Alloy

Susanne Obert[1], Alexander Kauffmann[1]*, Sascha Seils[1,2], Torben Boll[1,2], Sandra Kauffmann-Weiss[3], Hans Chen[4], Ronja Anton[5] and Martin Heilmaier[1]

[1]Karlsruhe Institute of Technology (KIT), Institute for Applied Materials (IAM-WK), Engelbert-Arnold-Straße 4, 76131 Karlsruhe, Germany

[2]Karlsruhe Nano Micro Facility (KNMF), Karlsruhe Institute of Technology (KIT), Hermann-von-Helmholtz-Platz 1, 76344, Eggenstein-Leopoldshafen, Germany

[3]Karlsruhe Institute of Technology (KIT), Innovation Campus Future Mobility (ICM), Kaiserstraße 12, 76131 Karlsruhe, Germany

[4]Karlsruhe Institute of Technology (KIT), Institute for Technical Physics (ITEP), Hermann-von-Helmholtz-Platz 1, 76344 Eggenstein-Leopoldshafen, Germany

[5]German Aerospace Center (DLR), Institute of Materials Research, Linder Hoehe, 51147 Köln, Germany

* corr. author: alexander.kauffmann@kit.edu; +49 721 608 42 346

Abstract

1 The oxidation behaviour of the pesting-resistant eutectic alloy Mo-20Si-52.8Ti was investigated by

2 addressing the microstructural and chemical constitution by grazing incidence X-ray diffraction GIXRD

3 and atom probe tomography APT of oxide scales formed at 800 and 1200 °C in order to understand their

4 protective character. The duplex Si-Ti-oxide scale formed at 800 °C in air, i.e. within the so-called

5 "*pesting regime*", is considerably slow growing with a scale thickness of (11 ± 3) µm after 1000 h of

6 exposure. It is composed of a Ti(+IV)-oxide with the chemical composition of approximately $TiO_{2.1}$

7 confirmed by APT and SiO_2 islands, which are most likely amorphous. The oxide scale formed at

8 1200 °C, a potential application temperature, is characterised by a top single-phase scale and an

9 underlying duplex scale with a considerably increased thickness of (68 ± 11) µm in total. It consists of

10 rutile TiO_2 and some cristobalite SiO_2 as determined by GIXRD. APT analysis of the top Ti-oxide scale

11 confirms the stoichiometry $TiO_{2.2}$. The underlying duplex scale comprising Ti- and Si-oxide is

12 characterised by strongly off-stoichiometric compounds, namely $TiO_{1.4}$ and $SiO_{1.6}$. Initial linear oxide

13 scale growth kinetics are found at 800 °C, which change to cubic kinetics for exposure times longer than

14 100 h. At higher temperatures of 1100 and 1200 °C, diffusion-controlled, almost parabolic kinetics

15 prevail.

Keywords

16 refractory alloys; oxide scale; microstructure; chemical composition; crystal structure; oxidation

17 kinetics

1. Introduction

The development of Mo-Si-based alloys for high-temperature applications as potential alternatives to state-of-the-art Ni-based superalloys is challenged by a judicious combination of sufficient creep resistance with adequate oxidation resistance. At elevated temperatures, this oxidation resistance can be achieved by: (i) Micro-alloying with B leads to a decrease in oxide scale viscosity [1] enabling quick coverage of the substrate surface by a borosilicate layer retarding further O ingress [2-4]. (ii) M_5Si_3 silicides with a higher Si content compared to M_3Si silicides (with M representing Mo or Ti, respectively) can be stabilised [5], which facilitate formation of a SiO_2 oxide scale [6]. However at temperatures below 1000 °C, catastrophic oxidation is characteristic for all Mo-Si-based alloys since the kinetics of SiO_2 formation is too slow in order to outbalance the formation of volatile MoO_3 leading to rapid mass loss [7, 8], called "*pesting*". Among multiple alloy design approaches, the ternary Mo-Si-Ti alloys were found to be the most promising regarding suppression of pesting [9]. A fully eutectic Mo-20Si-52.8Ti (at%) alloy possessing a two-phase, fine-scaled microstructure of Mo solid solution Mo_{SS} and $(Ti,Mo)_5Si_3$ was found *not* to undergo catastrophic oxidation at 800 °C [9]. An excellent oxidation resistance was observed with negligible specific mass changes in the order of 2 mg/cm^2 (isothermal) and 0.3 mg/cm^2 (cyclic) at 800 °C after 100 h [9]. This unexpected, outstanding oxidation behaviour has been attributed to the formation of a mixed SiO_2-TiO_2 layer with a scale thickness of less than 10 µm [9]. These observations were in striking contrast to the eutectoid Mo-Si-Ti alloy Mo-21Si-34Ti, being composed of Mo_{SS} and $(Mo,Ti)_5Si_3$, which suffered from severe pesting [9].

To summarise, our previous studies focused on the chemical and microstructural conditions for achieving pesting-resistance in eutectic-eutectoid Mo-Si-Ti alloys. It turned out that a threshold in nominal Ti content of minimum 43 at% is mandatory in order to obtain adequate oxidation resistance in the pesting regime [10, 11]. Moreover, it was found that the fine length scale of the eutectic microstructure is not required in order to achieve pesting-resistance since a considerably, artificially coarsened eutectic alloy exhibited a similarly good oxidation behaviour [11]. Thus, the chemical composition of the individual phases proved to be decisive whether pesting could be suppressed or not. While both M_5Si_3 silicides (with "M" being either Ti or Mo or a combination of both), hexagonal $(Ti,Mo)_5Si_3$ and tetragonal $(Mo,Ti)_5Si_3$, exhibit an adequate oxidation resistance in the pesting regime [12, 13], it is the pesting-critical Mo_{SS} phase which is responsible for the dominance of MoO_3 evaporation [11]. Continuous pathways of the Ti-oxide are present in the duplex scale connecting the alloy substrate with the outer TiO_2 oxide scale among all investigated Mo-Si-Ti alloys [10]. This is surprising with regard to the anticipated minor oxidation resistance of TiO_2, which is well known to exhibit scale cracking and spallation [14-17].

In conclusion, the reasons for the passivating character of the mixed Si-Ti-oxide scale formed on the eutectic alloy at 800 and 1200 °C, and especially the non-detrimental character of Ti-oxide still remain unclear. Therefore, this article addresses the crystallographic and chemical appearance of the oxide

53   scales and their growth characteristics. In particular, focus is placed on the solubility of the species Si,

54   Ti and Mo in the oxide phases by means of atom probe tomography (APT), in order to analyse its impact

55   on the pesting stability.

2. Experimental

56   The alloys were manufactured by repetitive arc-melting of the bulk high-purity elements Mo, Si and Ti

57   with purities of 99.95, 99.99 and 99.8 %, respectively. Therefore, an AM/0,5 device provided by

58   Edmund Bühler equipped with a button-shaped, water-cooled Cu crucible was used. Subsequent to

59   multiple evacuating ($< 2 \times 10^{-4}$ mbar) and Ar-flooding steps, a final Ar atmosphere of 600 mbar was

60   established, which was further cleaned from O residuals by pre-melting a Zr lump. Repetitive melting

61   (min. five times) ensured a homogenous element distribution. The resulting composition was confirmed

62   to vary less than 0.5 wt% from the initial nominal composition by inductively coupled plasma optical

63   emission spectroscopy.

64   Cyclic oxidation experiments were performed on samples with dimensions of $(5 \times 5 \times 4)$ mm^3 and a

65   surface finish of SiC grit P2500. Oxidation testing was conducted at laboratory air in muffle furnaces

66   by Carbolite Gero and Nabertherm at 800 and 1200 °C for a test duration in total of 1000 and 100 h,

67   respectively, with cycle durations varying between 1 to 10 h. The samples were cooled down to room

68   temperature between each cycle and their mass change was recorded by means of a balance (Sartorius

69   precision of $\pm$ 1 µg). The samples were maintained in Al_2O_3 crucibles during testing, but turned around

70   after each cycle to allow uniform oxidation of all surfaces.

71   The cross sections of the oxidation samples were analysed by scanning electron microscopy (SEM) after

72   representative oxidation durations. Therefore, the oxidation samples were cold mounted and prepared

73   by grinding steps down to SiC grit P2500 and subsequent polishing with 3 and 1 µm diamond suspension

74   and finally with stabilised silica suspension provided by Struers. A LEO EVO 50 SEM by Zeiss was

75   used at an acceleration voltage of 20 kV. Backscattered electron (BSE) imaging contrast, providing

76   atomic number and thus material contrast, allowed the characterisation of the oxide scale morphology.

77   The used SEM was equipped with an energy dispersive X-ray spectroscopy (EDX) system, which

78   allowed for an estimation of the chemical composition of the phases within the substrate. Quantitative

79   evaluation of the oxide scale thickness and the areal fractions of the respective oxides was performed

80   by applying image processing techniques, based on thresholding greyscale values and pixel connectivity

81   analysis using the software ImageJ and a self-written Matlab script.

82   In order to investigate the crystal structure of the formed oxide scales, grazing incidence X-ray

83   diffraction (GIXRD) analyses were performed. Therefore, a Rigaku SmartLab diffractometer was used,

84   equipped with a HyPix-3000 detector in 0D mode and a Cu Kα radiation source. The sample was aligned

85   by the usage of an Rx/Ry stage. The measurements were performed with a parallel beam and a 5° soller

86   slit in the primary beam path at incident angles ω varying between 1.2 and 2.5°.

87 Further analysis of the elemental distribution within the oxide scales was performed by means of 3D

88 atom probe tomography (APT). The tips from the oxide layers were prepared in a Strata dual beam

89 SEM/focused ion beam device by FEI. Firstly, the regions of interest were protected by a Pt layer to

90 avoid damage caused by the Ga^+ ion beam. Parts of an originally (25 x 4 x 3) μm^3 sized rod were set to

91 Si micro-posts provided by Cameca. Next, tips were shaped by annular milling at 30 kV with decreasing

92 inner diameter down to 0.2 μm. Final milling with a closed circular pattern was performed at 5 kV

93 acceleration voltage to minimize the Ga^+ affected layer at the surface.

94 Atom probe analyses were conducted in a LEAP 4000X HR by Cameca. The device was operated in

95 laser mode (UV laser with λ = 355 nm) at a pulse energy of 50 or 100 pJ and a pulse repetition rate of

96 100 or 125 kHz. The temperature was set to 50 K and the standing high voltage was controlled according

97 to a detection rate of 0.3 to 0.5 %.

98 Atom probe data were reconstructed and analysed by the IVAS 3.6.14 software by Cameca. The

99 chemical composition was determined using the peak deconvolution analysis to take the possible overlap

100 of peaks into account, especially, the overlap of TiO^{2+} and O_2^+ at 32 Da. Furthermore, APT analyses of

101 oxides, as well as carbides and nitrides, have shown that the quantification of the chemical composition

102 may depend on the experimental conditions [18-21]. An underestimation of the O content could be

103 caused by preferential co-evaporation of O or O-containing ions during the same laser pulse leading to

104 multiple signals on the detector, which cannot be separated [20]. Hence, a critical discussion of the

105 obtained compositions is necessary. It can be assumed that a possible O underestimation is consistent

106 for experimental conditions not varying substantially. These conditions are strongly influenced by the

107 evaporation field which depends on, e.g. the pulse energy, tip radius and material. Varying evaporation

108 fields can lead to significant changes in (i) the fraction of pulses leading to multiple signals and/or (ii)

109 the ratio of detected ions of the same species with different charge. The tips discussed in this article

110 exhibit about 80 % single signals and comparable ratios of ions at different charge states. Hence, similar

111 experimental conditions can be assumed for the APT investigations. Additionally, it was guaranteed that

112 no significant co-evaporation of O ions occurred during laser pulses. Therefore, a self-written software

113 by Boll et al. [22] was used to create separate mass spectra containing ions from single signals or

114 multiple signals, respectively. It was found that (i) the overall O content in the mass spectra derived

115 from multiple signals was lower than that from single signals and (ii) no disproportionally high amount

116 of O or O_2 ions occurred. Hence, it is unlikely that the APT analysis conditions cause a significant O

117 underestimation in the APT results.

118 The coefficient of thermal expansion (CTE) was determined by an optical dilatometer heating

119 microscope by LINSEIS. Here, the sample was compared to an Al_2O_3 reference during measurement.

120 The length difference was detected by a CCD camera. The CTE was analysed with a heating rate of

121 10 °C/min over the temperature range from 300 to 1200 °C under Ar flow of 3 sccm/min.

3. Results and discussion

In the following paragraphs we present structural (Sect. 3.1) and chemical investigations (Sect. 3.2) of the oxide scales formed on the eutectic Mo-20Si-52.8Ti alloy (at%) at 800 and 1200 °C. Thereafter, oxide scale growth kinetics will be evaluated in order to assess the rate-controlling processes (Sect. 3.3). In contrast to our previous article [10], where the distribution of the solid and volatile oxide forming species Ti, Si and Mo within the (sub-)oxide scales was evaluated, the evolution of the oxide scale thickness with time at different temperatures is focused on. In the following, oxides, in which Ti cations represent the major cationic component, are referred to as Ti-oxide, whereas oxides possessing majority Si cations as metal ions will be designated as Si-oxide. These terms are only meant as general, qualitatively distinction and are not to be misinterpreted by oxidation levels, or stoichiometry relations. These will be named and discussed where they are of particular interest (Sect. 3.2).

3.1. Structural characterisation of the oxide scales formed at 800 and 1200 °C

The general oxidation behaviour of the eutectic Mo-20Si-52.8Ti alloy has been studied in detail in Refs. [9, 11] for the as-cast and homogenised heat-treated condition with no significant differences in oxide scale formation and oxidation behaviour observed. Thus, we now focus on the detailed investigation and understanding of the formed oxide scales of the as-cast (ac) condition. The two-phase eutectic microstructure is differently fine-scaled and textured depending on the temperature profile during cooling after arc melting, and thus also partially degenerated (see Fig. 1: Mo_{SS} white and $(Ti,Mo)_5Si_3$ bright grey in BSE contrast). After being cyclically exposed to air at 800 °C for 100 h a thin duplex oxide scale of approximate (5 ± 2) µm in thickness is formed (see Fig. 1b), which grows to a thickness of (11 ± 3) µm after 1000 h of oxidation (see Fig. 1c). It consists of a Ti-oxide (grey in BSE contrast) with embedded islands of oxides rich in Si (dark-grey in BSE contrast) (see Fig. 1a to c). At 1200 °C after 100 h, a significantly thicker oxide scale (approximately 70 µm in total) is observed. Two distinct sub-scales are identified: (i) a single-phase, top Ti-oxide scale and (ii) a duplex scale comprising Ti- and Si-oxide underneath (see Fig. 1d and e). The duplex oxide scale was found to comprise a considerable fraction of Si-oxide of (52 ± 6) vol% [10]. The top Ti-oxide scale reveals a rather low porosity of (1.3 ± 0.2) vol%.
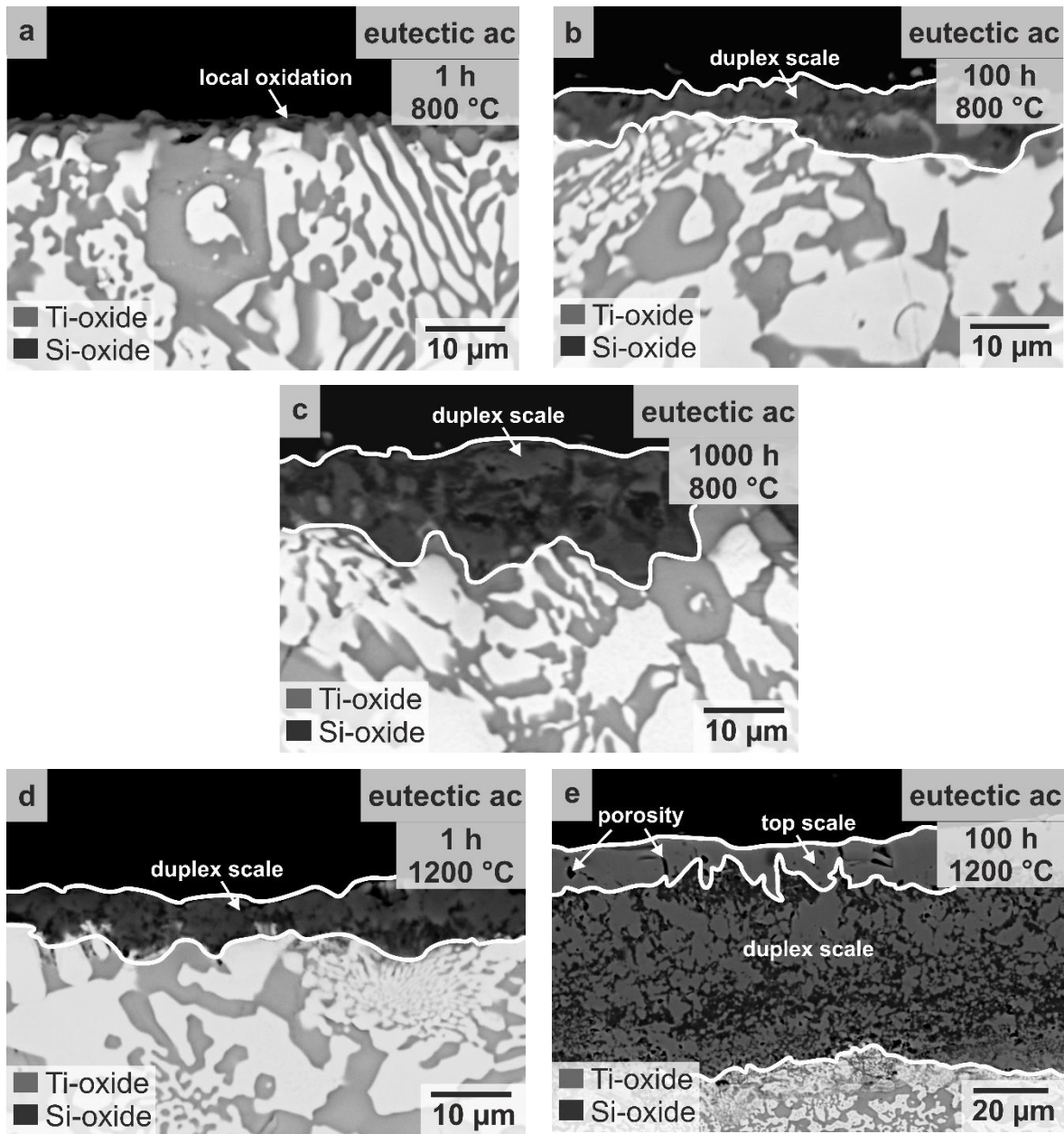
Fig. 1   BSE micrographs of the eutectic alloy Mo-20Si-52.8Ti after cyclic oxidation in laboratory air for 1, (a) 100 (b) and 1000 h (c) at 800 °C as well as 1 (d) and 100 h (e) at 1200 °C. Dark grey is the Si-oxide, while the Ti-oxide is light grey.

149 GIXRD measurements at an incident angle of $\omega = 1.2°$, presented in Fig. 2, confirmed the oxide scales

150 formed at 800 and 1200 °C to be mainly composed of rutile TiO_2, Ti(+IV)-oxide (space group P 4_2/m n

151 m) and small amounts of cristobalite SiO_2, Si(+IV)-oxide (space group P 4_1 2_1 1). Thus, with respect to

152 the considerable volume fraction of the (dark-grey) Si-oxide within the Si-Ti-oxide duplex scale formed

153 at 1200 °C (see Fig. 1e), it is expected that SiO_2 is mostly amorphous. This is in good agreement with

154 the results presented in Ref. [9] by electron back-scatter diffraction (EBSD). Besides, rutile TiO_2, some

155 peaks at $2\Theta = 26.78, 42.82, 63.04$ and $65.57°$ can be assigned to ordered TiO (space group C 1 2/m 1).

156 While the peaks at $2\Theta = 42.82, 63.04$ and $65.57°$ are either superimposed by $(Ti,Mo)_5Si_3$ (in the case of

157 the 800 °C oxidation sample), or cristobalite SiO_2, the peak at $2\Theta = 26.78°$ only matches the plane group

158 ($\bar{1}$11) of ordered TiO. However, more characteristic peaks of ordered TiO, for instance at $2\Theta = 30.29$,
159 or 46.74° of plane groups (111) and (021), respectively, would be expected, if a representative fraction
160 is prevalent in the oxide scale. Thus, the GIXRD results do not confirm the presence of TiO.
161 Additionally, some weak peaks at $2\Theta = 35.36, 39.85$ and 69.90° are assigned to the plane groups (410),
162 (501) and (621) of MoO_3 (space group P b n m). Note that the peak at $2\Theta = 69.90°$ is superimposed
163 by a rutile peak at 69.09° at 1200 °C. The detection of MoO_3 is attributed to re-deposition of volatile
164 MoO_3 on the oxide surface and partial incorporation into the growing oxide scale. Additionally, the
165 800 °C oxidation sample exhibits numerous peaks that can be assigned to $(Ti,Mo)_5Si_3$. This is reasonable
166 as the oxide scale possesses a rather low thickness and sub-oxide regions of the substrate were likely
167 detected even by GIXRD. This is confirmed by additional measurements with increasing incident angles
168 and therefore increased information depth, as the respective peaks become more pronounced (see Supp.
169 1 for GIXRD results with an increased incident angle of $\omega = 2.5°$). Furthermore, peaks corresponding
170 to bcc Mo_{SS} are not detected, which is in good agreement with the observations made by SEM analysis
171 (see Fig. 1a and b), showing that surface-near Mo_{SS} regions suffer from oxidation while the $(Ti,Mo)_5Si_3$
172 regions remain almost unaffected. Moreover, there are two weak peaks at $2\Theta = 24.67$ and 31.32° in the
173 GIXRD pattern of the 1200 °C oxidation sample, which cannot be assigned unambiguously. However,
174 these peaks neither correspond to the already discussed crystal structures, nor to further verified ones
175 (see Table 1).

Table 1 Examined crystal structures for evaluation of the GIXRD patterns (see Fig. 2).

| type	crystal structure	space group	matching peaks with GIXRD patterns
Ti-oxides	rutile TiO_2	P 4_2/m n m	yes
	ordered TiO	C 1 2/m 1	yes (superimposed by peaks of other crystal structures)
	NaCl-type TiO	F m $\bar{3}$ m	-
	monoclinic Ti_3O_5	C 1 2/m 1	-
	pseudobrookite Ti_3O_5	C m c m	-
	corundum Ti_2O_3	R $\bar{3}$ c	-
	anatase TiO_2	I 4_1/a m d	-
	brookite TiO_2	P b c a	-
Si-oxides	cristobalite SiO_2	P 4_1 2_1 1	yes
	rutile SiO_2	P 4_2/m n m	-
Mo-oxides	MoO_3	P b n m	yes
	VO_2-type MoO_2	P 1 2_1/c 1	-
	rutile MoO_2	P 4_2/m n m	-
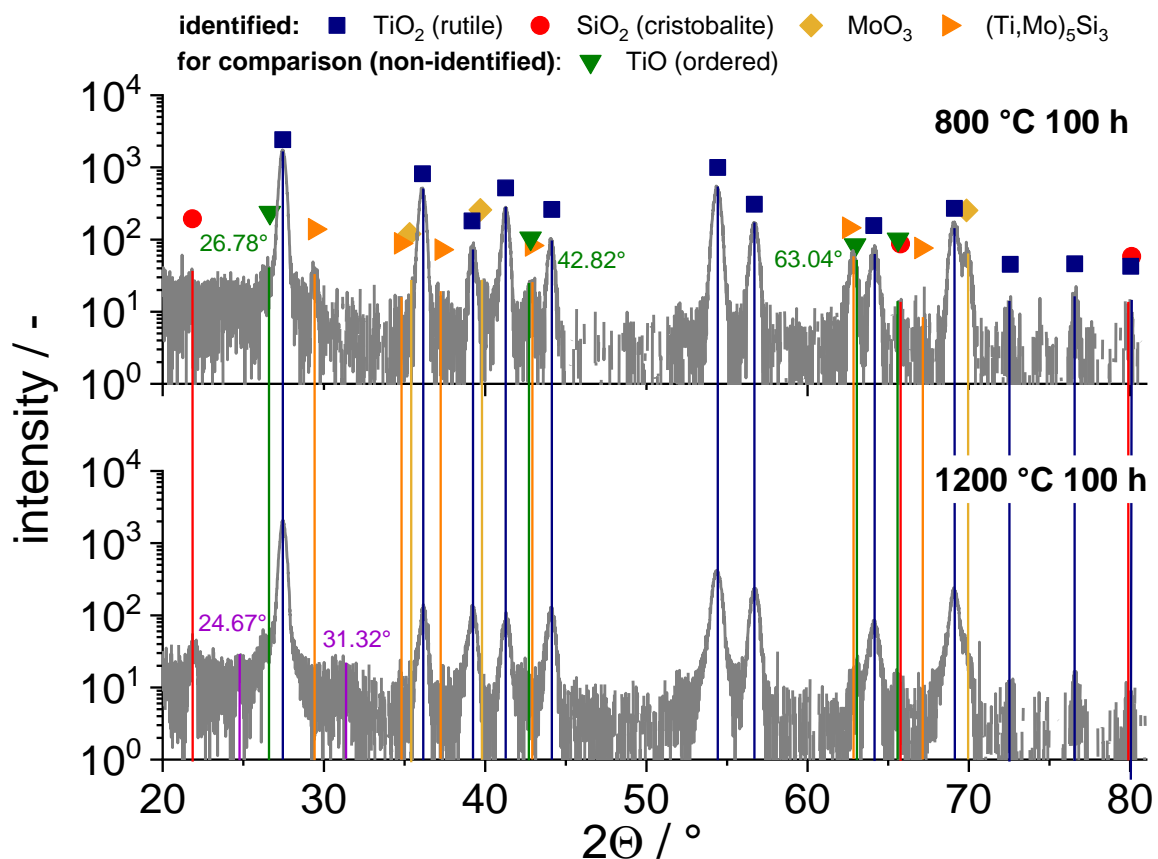
Fig. 2   GIXRD pattern of the surface of the oxidised sample at 800 (top) and 1200 °C (bottom) for 100 h. Note that the intensities are plotted in log scale. Diffraction angles that might correspond to ordered TiO (whose crystal structure cannot be identified unambiguously) are additionally labelled in green, whereas the non-assigned ones are labelled in violet colour.

3.2. Chemical analysis of the oxide scales formed at 800 and 1200 °C

176 The mass spectra of the investigated atom probe tips are displayed in Fig. 3, showing the characteristic

177 parts with the main peaks indicated. At 800 °C, the Si-oxide tip could not be evaluated due to instabilities

178 of tips manufactured from the oxide scale during APT analysis. Therefore, only the Ti-oxide tip was

179 analysed (see Fig. 3a). For the 1200 °C sample, three regions of interest were evaluated (compare to

180 BSE micrograph in Fig. 1e): (i) the top Ti-oxide scale (see Fig. 3b) and the underlying duplex scale of

181 both, (ii) the Ti- and (iii) the Si-oxide region (see Fig. 3c and d).

182 The mass spectrum of the Ti-oxide region formed at 800 °C (Fig. 3a) mainly exhibits TiO and TiO_2 as

183 well as O ion-related peaks. Additionally, the spectrum contains the main peak of Si^+ (28 Da) but no

184 side peaks or other O-containing Si peaks are identified. Furthermore, no peaks related to Mo are present,

185 which might have indicated the formation or incorporation of Mo-oxide. Thus, it can be concluded that

186 the peak at 32 Da predominantly results from TiO^{2+} ions. Nevertheless, the peak at 34 Da (a side peak

187 of O_2^+) indicates a significant contribution of O_2^+ to the peak at 32 Da, which has to be taken into account

188 for the determination of the chemical composition. After peak deconvolution the chemical composition

189 was found to be 34.4 at% Ti and 66.4 at% O (see Table 2), confirming the presence of TiO_2, Ti(+IV)-

190 oxide as already indicated by GIXRD analyses (see Fig. 2).

191 The mass spectrum of the top Ti-oxide region formed at 1200 °C (see Fig. 3b) exhibits similar peaks to

192 the spectrum of the 800 °C sample, except the ones for $Al^{+/2+}$ (27 and 13.5 Da) and AlO^{2+} (21.5 Da).

193 These peaks presumably result from a reaction with the alumina crucible during oxidation. The main

194 peak of Si^+ (28 Da) is identified as well and no Mo-related peaks are detected. Peak deconvolution

195 reveals the chemical composition to be 31.7 at% Ti and 68.3 at% O in the top Ti-oxide, 1200 °C sample

196 (see Table 2). Assuming no experimentally caused underestimate of the O content, (see Sect. 2), the

197 presence of TiO_2, Ti(+IV)-oxide, is confirmed in the top layer by APT. This was also expected from the

198 GIXRD analyses performed in this study (see Fig. 2) and from the EBSD results of the top Ti-oxide

199 scale revealing rutile TiO_2, see Ref. [9]. Although respective peaks are observed in the mass spectrum,

200 the concentration of Si and Al is below 0.1 at%.

201 The mass spectra of the Ti-oxide of the underlying duplex scale (see Fig. 3c) exhibits the same peaks

202 found in the mass spectra of the top layer tips, including a small Si^+ peak at 28 Da. Again, no Mo peaks

203 are observed and the duplex layer shows no peaks related to Al. The latter suggests that no reaction with

204 the alumina crucible has occurred during oxidation testing. This is reasonable as the duplex scale is

205 assumed to grow inwards and is separated from the atmosphere by the top Ti-oxide scale. Thus, it is not

206 in contact with the crucible. In comparison to the top Ti-oxide, 1200 °C sample, a lower O content of

207 only 59.0 at% (equiv. to 41.0 at% Ti) is determined after peak deconvolution. As discussed, it can be

208 assumed that the APT analysis conditions did not cause an underestimation of the O content. EBSD

209 analyses by Schliephake et al. [9] unambiguously confirmed the top oxide scale to be rutile TiO_2,

210 Ti(+IV)-oxide. However, in the underlying duplex scale, besides some rutile-assigned portions, multiple

211 un-indexed regions were assumed to be amorphous SiO_2. These un-assigned regions might represent

212 another Ti-oxide than rutile TiO_2, Ti(+IV)-oxide.

213 The mass spectrum of the Si-oxide (see Fig. 3d) mainly exhibits peaks, which can be assigned to Si and

214 O or combinations of both. Again, no Mo- or Al-related peaks are found. In contrast to all earlier

215 discussed mass spectra, the peak at 32 Da results predominantly from O_2^+ ions. Small side peaks of

216 TiO^{2+} ions can be observed at 31, 31.5, 32.5 and 33 Da. Using peak deconvolution, a total Ti content of

217 about 0.4 at% is obtained for the Si-oxide. The concentrations of Si (38.0 at%) and O (61.6 at%) are

218 close to the stoichiometry of Si(+IV)-oxide SiO_2, but this phase seems to be slightly depleted in O, too,

219 like the Ti-oxide in the duplex layer.

220 The corresponding subsets of the Ti-oxide, as well as of the Si-oxide regions within the duplex oxide

221 scale, which were taken to determine the chemical composition of the phases, are included in Fig. 3e.

222 The reconstructions of tip from the top Ti-oxide scales at 800 and 1200 °C are included in Supp. 2 for

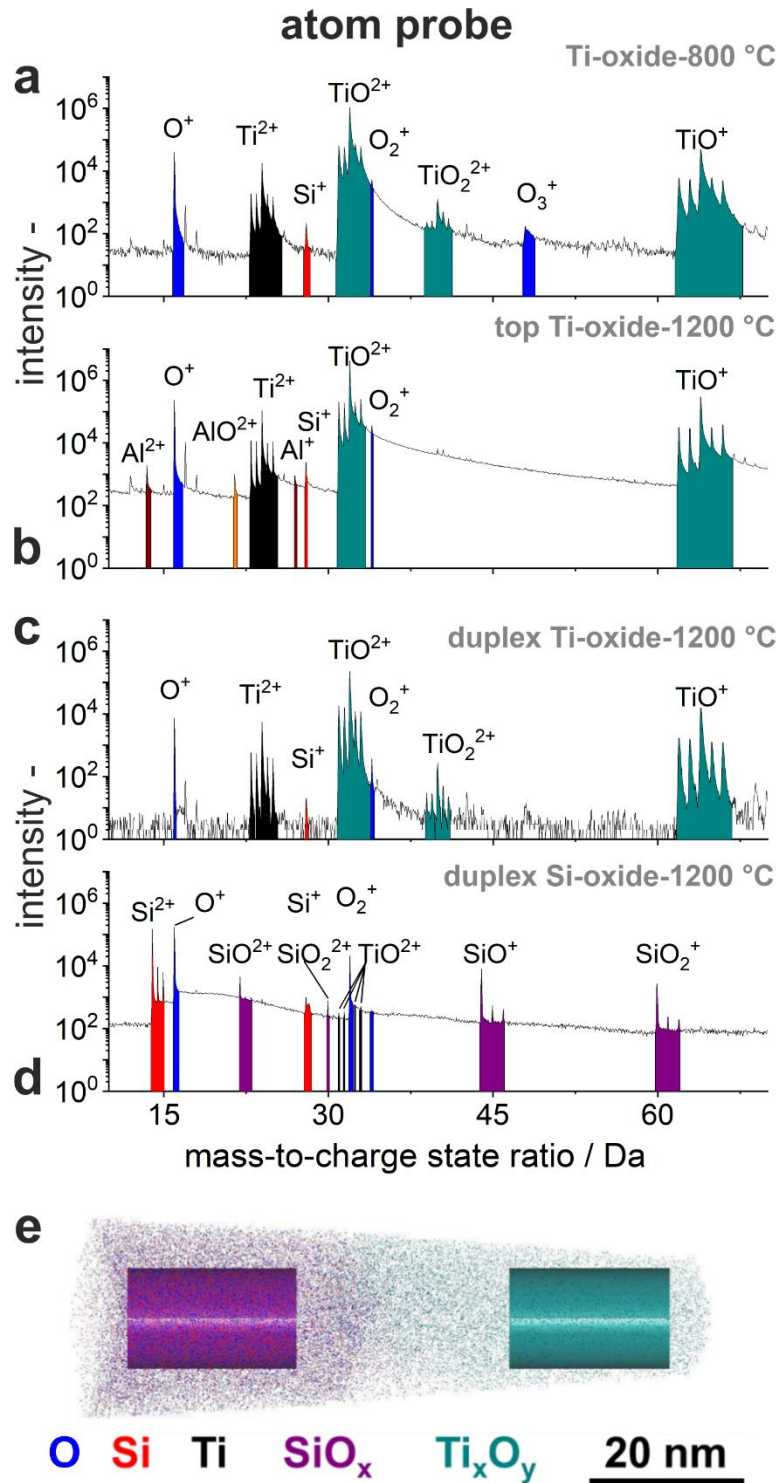223 the sake of completeness.

atom probe

Fig. 3   Characteristic parts of the mass spectra of the top layer of the Ti-oxide-800 °C sample (a), the top Ti-oxide-1200 °C sample (b), as well as the duplex Si-oxide-1200 °C (c) and the duplex Ti-oxide-1200 °C (d) regions of the duplex layer formed at 1200 °C. Corresponding visualisation of the subsets for the analyses of the duplex oxide scale at 1200 °C (e), for reasons of clarity only 1 % of all identified ions is shown here.

*Table 2   Chemical composition of the oxides in the investigated tips determined by APT after peak deconvolution (in at%) and comparison to the predominant oxide stoichiometry. * In this case, several presumable oxide stoichiometries are compared based on the experimental results.*

/ at%	Ti	Si	O	Al	predominant oxide	
Ti-oxide- 800 °C	32.4	< 0.1	67.6	-	$TiO_{2.1}$	Ti(+IV)
top Ti-oxide-1200 °C	31.7	< 0.1	68.3	< 0.1	$TiO_{2.2}$	Ti(+IV)
duplex Ti-oxide-1200 °C*	41.0	< 0.1	59.0	-	$TiO_{1.4}$	Ti(+II) or Ti(+III)
					$Ti_2O_{2.9}$	Ti(+III)
					$Ti_3O_{4.3}$	Ti(+IV/+III)
duplex Si-oxide-1200 °C	0.4	38.0	61.6	-	$SiO_{1.6}$	Si(+IV)

224   The experimental results of the Ti- and Si-oxide regions of the duplex scale are corroborated by literature

225   data proving that SiO_2 (Si(+IV)-oxide) and TiO_2 (Ti(+IV)-oxide) are in equilibrium at ambient pressure

226   in air at 1100 [23] and 1200 °C [24], respectively. Moreover, there is only a solubility of 0.85 at% Si in

227   rutile TiO_2 reported at 1300 °C for pressures of 3 GPa and higher [25]. Assuming a linear dependence

228   of solved Si in TiO_2 with pressure, a solubility at ambient pressure of less than 0.57 at% can be

229   extrapolated [25].

230   However, the unexpected stoichiometry and crystal structure of the Ti-oxide in the duplex scale at

231   1200 °C remains unsolved. As it is not clear what kind of oxidation level is prevalent in this oxide (see

232   Table 2, third row), for instance Ti(+II), Ti(+III) or Ti(+IV), the oxide is designated as Ti_xO_y with the

233   general description of the oxidation level Ti($+2y/x$). This off-stoichiometric Ti_xO_y is present as rutile

234   TiO_2 as confirmed by GIXRD in this work, because other crystal structure types cannot be assigned.

235   Additionally, the presence of rutile was confirmed by EBSD in Ref. [9], whereas sub-surface regions

236   are not indexed and might represent Ti-oxide other than rutile Ti(+IV)-oxide. However, the chemical

237   composition determined by APT is not in agreement with the stoichiometry range of stable rutile TiO_2

238   reported in literature (TiO_{2-x} with $x = 0$ to 0.04 [26, 27]). From a thermodynamic point of view, besides

239   TiO_2, the presence of Ti_3O_5 would be expected (solubility range Ti_3O_{5+x} with $x = 0$ to 0.1 [26, 28]) as

240   illustrated by the isothermal sections of the ternary Ti-Si-O (see Fig. 4a) and Mo-Si-O systems (see Fig.

241   4b) at the relevant temperatures of 1200 and 700 to 1000 °C, respectively. The possibly formed oxidation

242   products of the phases Mo_{SS} and Ti_5Si_3 (when neglecting the influence of dissolved Mo of (11 ± 3) at%

243   (determined by EDX) in $(Ti,Mo)_5Si_3$) can be seen when the O concentration (comparably to the oxygen

244   partial pressure) is increased (dotted line). A stability region of Ti_5Si_3, SiO_2 and Ti_3O_5 (highlighted in

245   blue in Fig. 4a) can be reached when Ti_5Si_3 is significantly enriched with O. With higher O concentration

246   or increased oxygen partial pressure, SiO_2 and TiO_2 are in equilibrium with O (highlighted in green in

247   Fig. 4a). Ti_4O_7 is here excluded, as it is not in equilibrium with $(Ti,Mo)_5Si_3$ and as the APT results do

248   not match the stoichiometry. During oxidation of Mo_{SS} the formation of MoO_2, SiO_2 and MoO_3 occurs

249   depending on the O concentration and oxygen partial pressure. Based on thermodynamics, it is likely

250   that at the substrate surface SiO_2 (solid) + Ti_3O_5 (solid) + MoO_3 (volatile) are forming, while the

11

251 composition of the duplex oxide scale of $SiO_2 + Ti_3O_5 + MoO_3$ (volatile) changes to SiO_2 and TiO_2 with

252 increasing thickness. The presence of the top TiO_2 oxide scale seems to be determined by the kinetics

253 due to its observed fast-growing nature [13, 29] and the fast diffusion of Ti cations within TiO_2 [30].
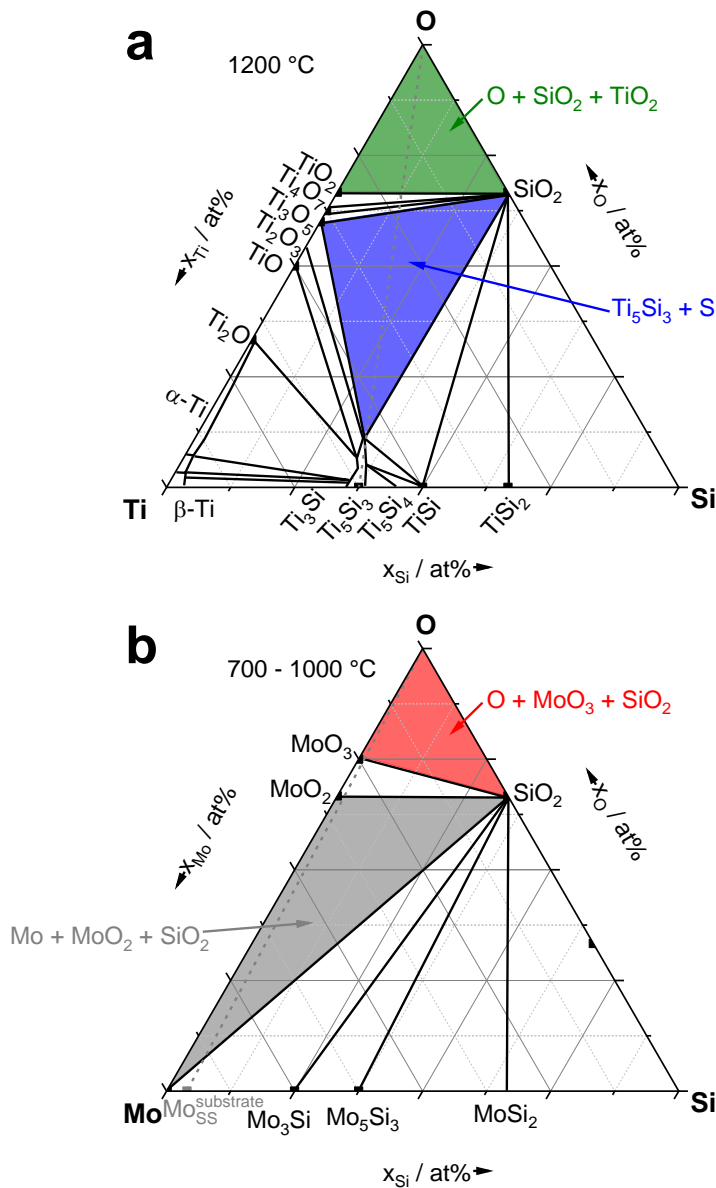

Fig. 4   Isothermal sections of the ternary Ti-Si-O (a) and Mo-Si-O (b) systems at 1200 and 700 to 1000 °C, respectively, including selected, highlighted phase equilibria along the stability line of Ti_5Si_3 or Mo_{SS} (dotted grey line) with enrichment of O [23, 31].

3.3. Analysis of the oxidation kinetics

254 In the following, the oxidation kinetics will be referred to as the kinetics of oxide scale growth, if not

255 otherwise stated. Literature data on weight change oxidation kinetics, which are considered for

256 comparison, are explicitly highlighted.

257 The evolution of the (sub-)oxide scale thickness d (internal oxidation d_{int}, duplex d_{duplex} and top scale

258 d_{top}) at 1200 °C is plotted in Fig. 5a as a function of time in double logarithmic manner (data at 100 h

259 taken from our previous article [10]). The following power fit function for the oxide scale thickness d

12

260   in dependence of the exposure time t with the oxidation rate constant k_n for a specific exponent n was

261   applied:

$$d^n = k_n \cdot t \qquad\qquad \text{Eq. 1}$$

262   First, the fit was performed with the exponent n being fixed to 2, which is equal to a parabolic oxide

263   scale growth law [32]. Additionally, n was adjusted individually in order to achieve optimum fit quality

264   for comparison (dotted fit lines in Fig. 5a). It is revealed that: (i) The overall oxide scale growth at

265   1200 °C is dominated by the growth of the duplex scale (green circles). (ii) Both, the evolution of the

266   oxide scale in total d_{total} (violet triangles) and the duplex scale d_{duplex} (green circles) are parabolic

267   with n values close to 2. (iii) Subtraction of the duplex scale data from the total oxide scale yields the

268   change of the top single-phase oxide scale with time (blue triangles), which also seems to follow a

269   parabolic rate law. However, a fit itself for the data points of the top single-phase was not possible since

270   only two data points could be validly determined as for short oxidation times no separation of a top

271   single-phase oxide scale was observed. In conclusion, the oxidation kinetics are determined to be

272   parabolic and thus, the oxidation mechanism is regarded as bulk diffusion rate-controlled by either the

273   oxidant (O anion) or the reactant (metal cation) through the (sub-)oxide scales.

274   In order to assess whether there is a change in oxidation mechanism with decreasing temperature and

275   thus, less thermal activation for diffusion processes, the evolution of the total oxide scale thickness

276   d_{total} at 1200 °C is compared to the observations made at 800 and 1100 °C (see Fig. 5b). It is

277   demonstrated that the oxide scales are considerably thicker at elevated temperatures, namely (26 ± 7)

278   and $(68 \pm 11)\,\mu m$ at 1100 and 1200 °C, respectively, as compared to only $(5 \pm 2)\,\mu m$ at 800 °C after

279   100 h of cyclic oxidation. Moreover, it is found that the oxide scale evolution might be associated with

280   an almost cubic oxidation kinetics at 1100 °C as well, as revealed by an exponent of $n = 2.94$ (see Table

281   3). The cubic and parabolic growth observed at 1100 and 1200 °C, respectively, is attributed to diffusion

282   processes, especially relevant at high temperatures. This is confirmed by the estimated diffusion distance

283   of Ti^{4+} cations in TiO_2, Ti(+IV)-oxide at the respective temperatures, which is found to be 29 and 62 µm

284   after 100 h at 1100 and 1200 °C, respectively, which is in excellent agreement to the experimental

285   values. The impact of the temperature on the evolution of the oxide scale thickness is underlined by Fig.

286   5c. The dependence of the total oxide scale thickness is highlighted as a function of temperature for

287   specific exposure durations of 1, 10 and 100 h.

288   In contrast, the overall evaluation of the oxide scale growth at 800 °C does not yield parabolic kinetics,

289   even after exposure times of 1000 h, as a considerably increased exponent of $n = 4.45$ according to Eq.

290   1 is noted. Such high exponents in power-law oxidation kinetics are neither widely reported, nor

291   discussed in literature. Additionally, as only a moderate fit quality ($R^2_{adj} = 0.82$) is obtained, it is

292   suggested that there are different oxidation stages with changing oxidation kinetics. This suggestion is

293   supported by considering the initial oxidation stage up to 100 h and the ongoing stage from 100 to 1000 h

separately. During the initial oxidation stage, it is likely that the prevalent oxidation mechanism is reaction rate-controlled, as a linear fit leads to an excellent fit quality with $R^2_{adj} = 0.97$ (see Table 3). The obedience to linear oxidation kinetics is further corroborated by the discontinuous morphology of the oxide scale for exposure times shorter than 100 h (see BSE micrographs in Fig. 1). It is shown that the oxidation occurs locally, especially in the surface-near Mo_{SS} regions, although not providing full coverage of the alloy substrate (see Fig. 1a and b). Therefore, the kinetics up to 100 h are most likely to be rate-determined by surface reactions occurring either at the oxide scale/atmosphere interface or at the oxide scale/substrate interface. Other oxidation mechanisms leading to linear oxidation kinetics, such as direct O access to the substrate through porous oxide scales or cracks, are unlikely, since neither significant porosity nor cracks are observed in the oxide scale by SEM analysis (see Fig. 1a and b). Note that this initial linear oxidation kinetics does not lead to catastrophic oxidation behaviour, as the oxidation rate constant of 8.25 x 10^{-12} ms^{-1} is significantly low. For longer exposure times than 100 h, a continuous mixed Si-Ti-oxide scale is formed (see Fig. 1c), which accounts for the change in oxidation kinetics. Fitting the respective values according to Eq. 1 leads to an exponent of 3.18 with a good fit quality of $R^2_{adj} = 0.94$. This reveals that the oxidation kinetics change from linear to cubic. In literature, cubic oxidation kinetics are assumed to be determined by diffusion processes along grain boundaries [33-35]. Thus, it might be that O inward diffusion along grain boundaries and Ti-oxide/Si-oxide phase boundaries determines the oxidation mechanism for exposure times longer than 100 h. However, no profound evidence can be given here for this assumption.
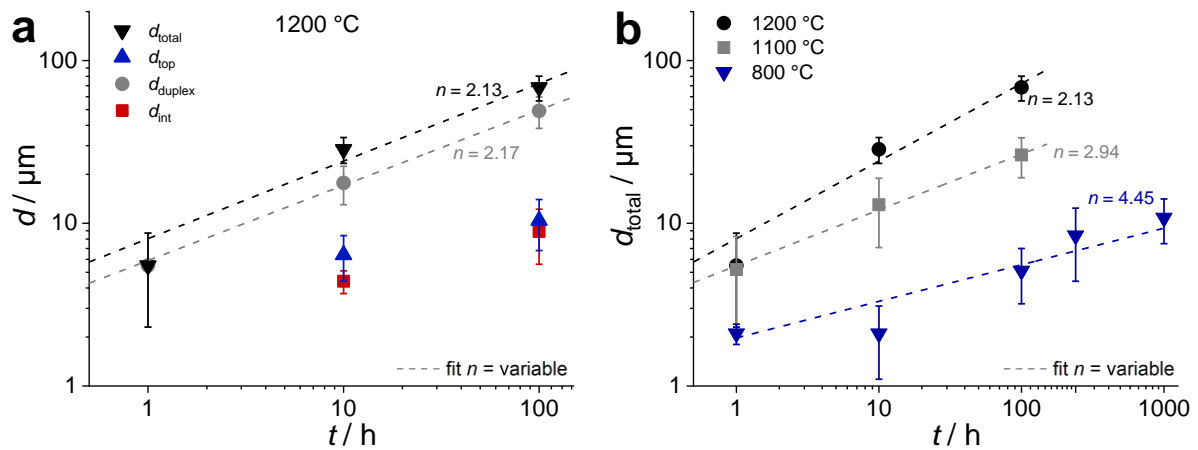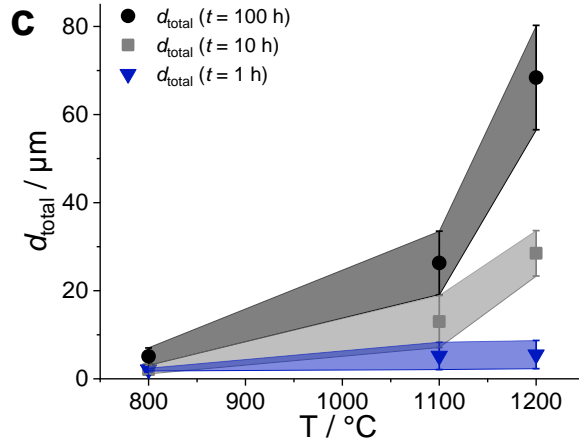
Fig. 5   Evolution of the oxide scale thickness in total d_{total} and of the respective sub-scales (top Ti-oxide d_{top}, duplex Si- and Ti-oxide scale d_{duplex} and internal oxidation zone d_{int}) in dependence of the exposure time t at 1200 °C for the eutectic alloy (a). Fit functions according to Eq. 1 with n being adjusted variably (dotted lines) are included. In comparison d_{total} is displayed logarithmically at 800, 1100 and 1200 °C (b) and fitted accordingly as well (b). The total oxide scale thicknesses are compared for different times at 800, 1100 and 1200 °C (c).

Table 3   Determined oxidation rate constants k_n for 800, 1100 and 1200 °C. For 1100 and 1200 °C referring to Eq. 1. For 800 °C k^*, referring to a linear fitting method, is included. R^2_{adj} values are provided as well.

T / °C	fitting range of t / h	n / -	k_n / $m^n s^{-1}$	k^*/ ms^{-1}	R^2_{adj} / -
800	1 – 1000	4.45	1.16 x 10⁻²⁹	-	0.82
	1 – 100	1 (linear)	-	8.25 x 10⁻¹²	0.97
	100 – 1000	3.18	4.51 x 10⁻²³	-	0.94
	100 – 1000	2 (parabolic)	4.41 x 10⁻¹⁷	-	0.61
1100	1 – 100	2.94	8.64 x 10⁻²⁰	-	0.99
		2 (parabolic)	2.38 x 10⁻¹⁵	-	0.86
1200	1 – 100	2.13	3.56 x 10⁻¹⁵	-	0.96
		2 (parabolic)	1.51 x 10⁻¹⁴	-	0.96

313   The high-temperature parabolic oxidation behaviour of the eutectic alloy Mo-20Si-52.8Ti is

314   characterised by the parabolic oxidation rate constant $k_{n=2}$ = 2.38 x 10⁻¹⁵ (1100 °C) to 1.51 x 10⁻¹⁴ $m^2 s^{-1}$

315   (1200 °C), which are thermally activated with an activation energy of 310 kJ/mol. These findings also

316   apply to certain eutectic-eutectoid alloys from Ref. [11] (see App. 1 for their chemical compositions),

317   as well as to the eutectoid alloy from Ref. [9], as parabolic oxidation kinetics with similar oxidation rate

318   constants to the eutectic alloy were revealed with activation energies in the range of 200 to 410 kJ/mol.

319   Note that the determination of these activation energies is based on only two data points and thus, only

320   serves as estimates when interpreting the activation energies.

321   Moreover, no difference was found between the pesting-resistant and non-pesting-resistant Ti-rich and

322   Ti-lean (nominal Ti content < 43 at%) alloys, respectively, which could have been taken into

323   consideration for further understanding the root causes of pesting resistance. However, in order to

15

classify the oxidation behaviour of these Mo-Si-Ti alloys, their parabolic oxidation rate constants $k_{n=2}$ are compared to the relevant diffusion coefficients of this systems. Since the oxidation rate constants are known to be thermally activated [36], these can be visualised by an Arrhenius plot in Fig. 6. The following correlation between the oxidation rate constant and the diffusion coefficient D allows a direct comparison of the respective diagrams (see Eq. 2 [37]):

$$k_{n=2} = \frac{2\,D\,C_0}{N}$$

Eq. 2

Here, D is the diffusion coefficient of a specific species diffusing in the oxide, C_0 is the oxidant concentration at the scale surface and N is the number of oxidant species incorporated in the newly grown oxide of unit volume [37].

Generally, it is seen in Fig. 6 that Ti ion diffusion (solid blue line) is considerably faster than O ion diffusion in TiO$_2$ (dotted, dashed and solid red lines). This is in good agreement with the assumption that the top Ti-rich oxide scale is growing outward by Ti-cation outward diffusion, which has also been experimentally verified by marker experiments by Azim et al. in Ref. [29] on Mo-Si-B-Ti alloys. In contrast, the diffusion coefficient for Si bulk diffusion in SiO$_2$ is significantly lower compared to the diffusion coefficients for O. This is in accordance with the assessment of Deal and Grove in Ref. [38] who stated that SiO$_2$ formation proceeds rather by the inward diffusion of O, than by the outward diffusion of Si. Furthermore, the respective oxidation rate constants of the eutectic alloy ($k_{n=2}^{eutectic}$), of the intermediate eutectic-eutectoid alloys ($k_{n=2}^{eutectic-eutectoid}$) and of the eutectoid alloy ($k_{n=2}^{eutectoid}$) are found to be in the range of the diffusion coefficient of Ti in TiO$_2$. Hence, it can be concluded that the oxidation rate of these eutectic-eutectoid Mo-Si-Ti alloys is determined by the Ti diffusion in TiO$_2$.
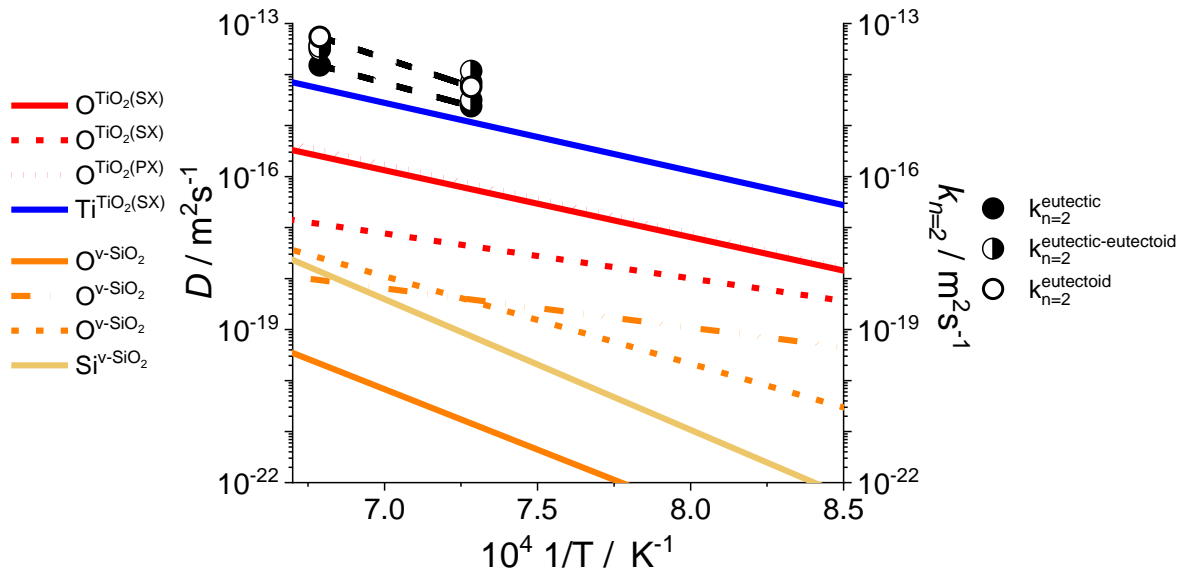

Fig. 6   *Temperature-dependence of the diffusion coefficients D of Ti and O ions in single-crystalline (SX) and polycrystalline (PX) TiO$_2$ (blue and red lines) and Si- and O ions in vitreous (v) SiO$_2$ (yellow and orange lines), respectively. Data taken from [39-44]. For comparative reasons, the values of $k_{n=2}$ for the eutectic (black solid circle), eutectic-eutectoid (half-opened circles) alloys and the eutectoid alloy (open black circle) are added.*

In order to understand the observed oxidation kinetics in the Mo-Si-Ti system, the individual oxidation behaviour of the constitutional phases Mo_{SS} and $(Ti,Mo)_5Si_3$ will be discussed in the following. Mo is known to undergo catastrophic oxidation due to volatilisation of MoO_3 at temperatures above 500 °C [45-47]. The respective activation energy for temperatures beyond 800 °C was associated with a diffusion-controlled process through the gas phase [45, 47, 48] with 82 kJ/mol [45]. However, the tendency of forming volatile MoO_3 can be counterbalanced by the formation of solid Ti-rich oxides, when alloyed with Ti [11]. Thus, the linear mass loss oxidation rate can be considerably decelerated at 800 °C, namely from -33 to -14 mg/cm^2h^{-1}, when increasing the Ti content from 20 to 40 at% [11]. The here discussed eutectic alloy comprises a Ti-rich Mo_{SS} with an approximate Ti content of 45 at% [10]. This supports the observed pesting-resistance in Ti-rich Mo-Si-Ti and Mo-Si-B-TiC alloys at 800 °C with considerable volume fractions of Ti-containing Mo_{SS} [10, 11, 49]. Therefore, the improvement in oxidation behaviour is attributed to the formation of a (relatively) dense TiO_2 oxide scale [49].

In comparison, the silicide phase Ti_5Si_3 reveals different weight change oxidation kinetics, which are dependent on the Si content and the oxidation duration [50]. The $(Ti,Mo)_5Si_3$ phase present in the investigated eutectic alloy exhibits a constant Si ratio close to the ideal stoichiometry due to ingot metallurgical manufacturing. Furthermore, there is a considerable Mo concentration of (13 ± 4) at% [11]. Therefore, the phase composition is regarded to be comparable to the studies made by Majumdar et al. in Ref. [12] on an Mo-30Si-40Ti alloy, which comprises a $(Ti,Mo)_5Si_3$ matrix, but with an increased Mo content of 26 at%. The oxidation behaviour was reported to obey parabolic weight gain and oxide scale growth kinetics in the temperature range of 900 up to 1300 °C [12]. Thereby, the formation of an outer TiO_2 scale and an underlying SiO_2-TiO_2 duplex scale was observed [12] like for the investigated Mo-Si-Ti alloys from the present study (the eutectic alloy Mo-20Si-52.8Ti, as well as the other derivatives from the Mo-Si-Ti system listed in App. 1). The authors concluded that the formation of volatile MoO_3 is suppressed in $(Ti,Mo)_5Si_3$ [12]. The parabolic oxidation rate constant was found to be about half an order of magnitude lower than in the eutectic alloy at 1200 °C in Ref. [12] (compare with Table 2). The corresponding activation energies were determined to be 72 and 325 kJ/mol in the temperature range between 900 to 1200 °C and 1200 to 1300 °C, respectively [12]. This first seems comparably low, but was interpreted by the authors on the basis of the activation energy for diffusion of oxygen in fused SiO_2 which was regarded to be in the same order [12]. At higher temperatures instead, the activation energy is comparable to the activation energies found for the Mo-Si-Ti alloys in this study (see App. 1). The difference in activation energies was attributed to a change in microstructural set-up of the duplex oxide scale with an increased volume fraction of TiO_2, which might lead to accelerated O inward diffusion [12]. Conclusively, $(Ti,Mo)_5Si_3$ exhibits a diffusion-controlled oxidation behaviour, which is mainly attributed to the inward diffusion of O through the SiO_2-TiO_2 duplex scale [12].

This comparative study reveals that the oxidation kinetics are combined kinetics of the constituting phases Mo_{SS} and $(Ti,Mo)_5Si_3$. At high temperatures the diffusion processes are fast enough to form

379 continuous, solid oxide scales, which can be accounted for the parabolic bulk diffusion-controlled

380 oxidation, comparable to the oxidation kinetics of $(Ti,Mo)_5Si_3$. By contrast, the oxidation kinetics at

381 800 °C are different to the ones observed for the constituting phases Mo_{SS} and $(Ti,Mo)_5Si_3$, as the

382 eutectic alloy reveals linear oxidation kinetics at the beginning, turning into cubic kinetics for oxidation

383 times longer than 100 h.

384 These fundamental differences might be rationalised as follows: Generally, the defect structure of the

385 oxide determines the oxidation kinetics. In the case of rutile TiO_2 the defect structure depends on

386 temperature, oxygen partial pressure, the exact stoichiometry [51] and impurities [52]. At 1100 and

387 1200 °C, the main defects are O vacancies and Ti cations of different valences (Ti^{3+}, Ti^{4+}) [53]. While

388 the first primarily contribute to the non-stoichiometry [53, 54], the latter are the defects dominating scale

389 formation.

390   *3.4. The role of the Ti-oxide within the oxide scales formed on the eutectic alloy Mo-20Si-52.8Ti*

391 The good oxidation resistance of the Ti-oxide formed on the eutectic alloy Mo-20Si-52.8Ti (see Fig. 1)

392 in comparison to pure Ti is unexpected [36, 55]. Therefore, possible explanations are discussed in the

393 following: In essence, the oxidation resistance of Ti is improved by reducing its O solubility [55], e. g.

394 by alloying with Al or Si [16, 56]. A reduction in oxidation rate is attained in Ti-xSi alloys with $x = 0.4$

395 to 1.7 or 12.7 at% Si at 500 to 700 and 850 °C, respectively [16, 56]. Moreover, a parabolic oxidation

396 behaviour is observed for Ti-Si alloys in contrast to a linear one, which is present in pure Ti [56]. When

397 3.3 at% Si or less are added, Si was found to be homogenously distributed within the oxide scale, either

398 solved as solid solution in rutile TiO_2 or as embedded SiO_2 islands with diameters of less than 1 µm at

399 850 °C [56]. In contrast, higher additions up to 13 at% Si were found to be inhomogeneous distributed

400 within the oxide scale and even led to cracking at the substrate/oxide interface [16]. Hence, the Si

401 concentration presumably accounts for a transition in oxide scale morphology preventing pore formation

402 and spallation, which typically occurs in TiO_2 formed on pure Ti [56]. There are several impacts of Si

403 on the oxidation behaviour of Ti-Si alloys proposed: (i) Si might retard the inward diffusion of O and

404 therefore lead to a reduction in penetration depth [56], as interstitially solved Si ions might reduce the

405 amount of available O vacancy sites decelerating the diffusion rate of O in rutile TiO_2 [56]. (ii) The

406 presence of SiO_2 facilitates the formation of a denser, less porous oxide scale and prevents

407 recrystallisation and stratification of TiO_2 due to the change in stress relaxation processes within the

408 oxide scale [16, 56]. However, it is questionable whether the very low amount of Si/SiO_2 in TiO_2/Ti-

409 oxide below 0.1 at% formed on the eutectic alloy (see Table 2 and Fig. 2) can be taken into account for

410 a reduction in O vacancies due to preoccupation by Si ions. For comparison, in Ti-Nb alloys, solution

411 of Nb^{5+} ions was observed in rutile TiO_2 leading to a significant deceleration of oxide scale growth at

412 900 and 1000 °C in static air [57]. Thereby, Nb^{5+} ions were found to substitute Ti^{4+} ions with an

413 estimated ratio of less than 0.14 % [57].

414   Although, TiO_2 formed on Ti or Ti-based alloys often suffers from cracking [16, 55, 58-60], the oxide

415   scales (especially the Ti-oxide) formed on the eutectic alloy are crack-free with very low porosity of

416   less than 1.5 vol% along the oxide scale substrate interface [11]. This indicates that a change in density

417   and adherence of the oxide scales allow for the high oxidation resistance. The crack formation is often

418   caused by the formation of sub-layers like TiN [16], but none were observed on the current eutectic

419   alloy Mo-20Si-52.8Ti. Moreover, the mismatch of the CTE needs to be considered with regard to the

420   oxide/substrate compatibility. For this purpose, CTE values are compared in Table 4. There is no

421   considerable difference in CTE, no matter whether TiO_2 is growing on Ti or on the eutectic alloy.

422   However, especially at longer exposure times and higher temperatures, the relationship between the top

423   TiO_2, the duplex scale and the eutectic alloy substrate has to be taken into account. The CTE of thermally

424   grown SiO_2 is about one order of magnitude lower, so it is likely that the SiO_2 portions balance the

425   thermal expansion of TiO_2 within the (duplex) oxide scale and suppress crack formation during cyclic

426   oxidation testing.

427   *Table 4 Comparison of the coefficients of thermal expansions (CTE) of Ti, TiO_2, SiO_2 and the eutectic alloy Mo-20Si-52.8Ti.*

	CTE / K^{-1}	Refs.
Ti	10.5×10^{-6} (20 – 700 °C)	[61]
TiO_2	*a*-axis: 8.1×10^{-6} (276 °C) *c*-axis: 10.6×10^{-6} (276 °C)	[62]
SiO_2	5×10^{-7} (RT – 300 °C)	[63]
eutectic alloy	$7.0 – 9.1 \times 10^{-6}$ (300 – 1200 °C)	this study

428   In conclusion, the beneficial impact of the Ti-oxide on the oxidation behaviour is attributed to the

429   interaction with the Si-oxide, which might lead to a reduction in available vacancies for O inward

430   diffusion. Additionally, with regard to the diffusion of O, Si and Ti, the O concentration being available

431   for the formation of the duplex oxide scale at 1200 °C is determined by the O ion diffusion flux through

432   the top TiO_2 oxide scale. Once the duplex scale is formed, Ti ion diffusion (which might be faster along

433   the penetrating Ti-oxide regions through the oxide scale) to the top TiO_2 scale is necessary for further

434   growth of the top TiO_2 oxide scale. Therefore, it is concluded that the fast formation of the top TiO_2

435   scale is triggered by kinetics and that its growth is slowed down with ongoing formation of the

436   underlying duplex scale.

4. Summary and Conclusion

437   The analysis of the microstructural constitution of the oxide scales formed on the eutectic Mo-20Si-

438   52.8Ti alloy at 800 °C revealed a single-layered mixed oxide scale comprising Ti- and Si-oxide. At

439   1200 °C, a top Ti-oxide scale with an underlying mixed duplex Ti- and Si-oxide scale is observed.

440   Besides rutile TiO_2 and some cristobalite SiO_2, GIXRD analyses indicate the presence of some MoO_3

441   in the oxide scale formed at 1200 °C. However, the formation of MoO_3 is outbalanced and

overcompensated by solid oxide scale formation as documented by negligible mass changes even after test durations of 100 h. The assessment of the compositional constitution of the oxide scales by APT leads to the following conclusions: (i) The chemical composition of the (top) Ti-oxide scales formed at 800 and 1200 °C is found to be comparable with a stoichiometry matching rutile-type TiO_2 Ti(+IV)-oxide. (ii) The duplex scale formed at 1200 °C is composed of an O-depleted Ti-oxide region off-stoichiometric to typical known Ti-oxide, among which Ti_3O_5 is the most likely one to be present. (iii) The Si-oxide region within the duplex scale is depleted in O as well, with a stoichiometry of $SiO_{1.6}$ closest to SiO_2. It is unlikely that this observed depletion in O is caused by an underestimation caused by the measurement conditions. (iv) Virtually no solubility of Mo is found in the Ti- and Si-oxide, respectively, for both oxide scales formed at 800 and 1200 °C. (v) There is a negligible amount of Si solved in the Ti-oxide formed at 800 and 1200 °C.

The study of the oxide growth kinetics revealed that the oxide scale growth obeys a linear rate law at 800 °C up to 100 h pointing to a surface reaction-controlled oxidation. Longer exposure times facilitate the formation of a continuous mixed oxide scale, which results in cubic oxidation kinetics. In contrast, at 1100 and 1200 °C the thickness of the overall oxide scale and of the duplex scale grows with almost parabolic oxidation kinetics. This is also found for the eutectoid and eutectic-eutectoid Mo-Si-Ti alloys. The activation energies of the parabolic oxidation rate constants are in good agreement with published data on activation energies for self-diffusion of O, Ti and Si in the respective oxides [39-44, 64] confirming the oxidation rate to be diffusion-controlled. The observed change in oxidation mechanism between 800 and 1100 °C correlates with the oxidation kinetics of the microstructural constituents Mo_{SS} and $(Ti,Mo)_5Si_3$. While Mo_{SS} is known to undergo catastrophic oxidation with linear mass loss [45, 46], which is decelerated with increasing Ti content [11], above 600 °C, $(Ti,Mo)_5Si_3$ was found to obey parabolic oxide growth kinetics in the temperature range of 900 to 1300 °C [12].
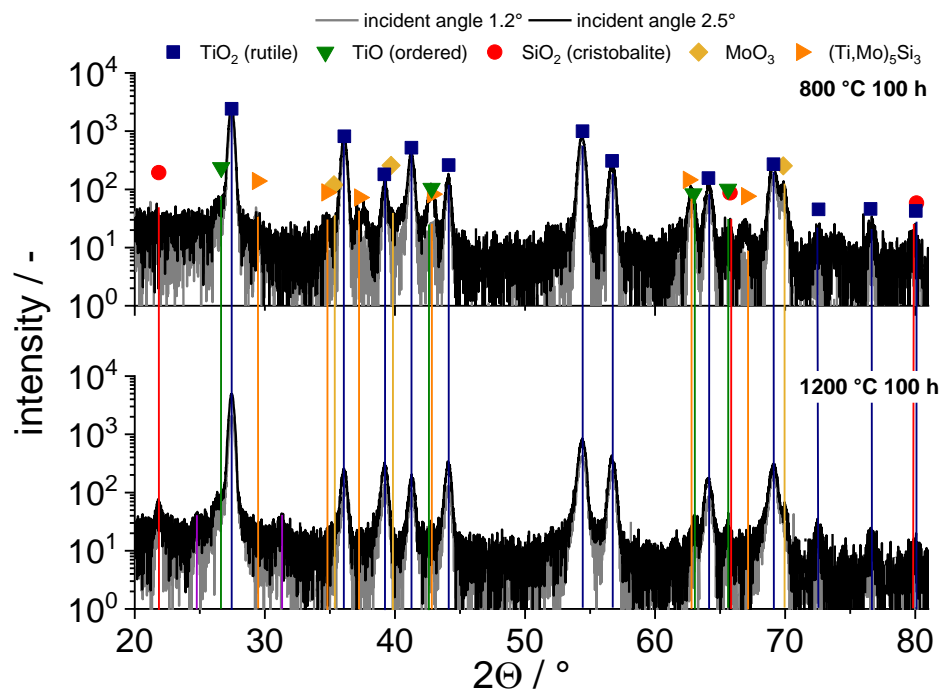
Appendix

App. 1   Nominal chemical composition of eutectic-eutectoid Mo-Si-Ti alloys corresponding to Refs. [9, 11].

| eutectic-eutectoid alloys	nominal composition / at%
alloy #1	Mo-21Si-47Ti
alloy #2	Mo-21Si-43.4Ti
alloy #3	Mo-21.5Si-41.5Ti
alloy #4	Mo-21Si34Ti

Supplementary

Supp. 1   GIXRD diffraction patterns of the cyclically oxidised samples at 800 (top) and 1200 °C (bottom) for 100 h with incident angles of 1.2 (grey) and 2.5° (black). Note that the intensities are plotted with logarithmic scale.
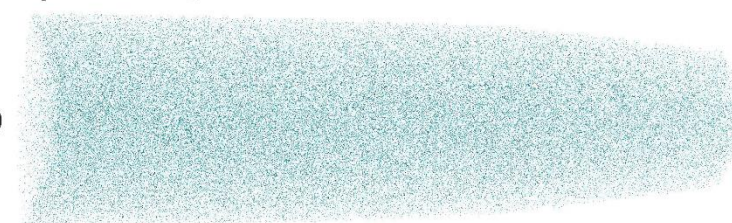
top Ti-oxide, 800 °C

a
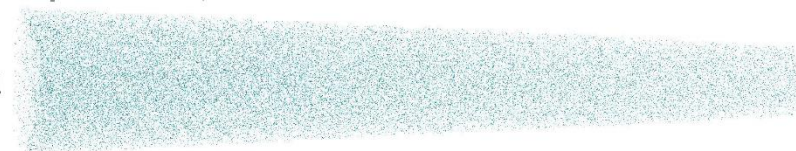
top Ti-oxide, 1200 °C

b

O   Si   Ti   Ti$_x$O$_y$ ___50 nm___

Supp. 2 Visualisation of the subsets for the APT analyses of the top Ti-oxide scale at 800 (a) and 1200 °C (b). For reasons of clarity only 1 % of all identified ions is shown here. No SiO$_x$ ions were identified.

Data availability statement

The raw and processed data required to reproduce these findings are available on request to alexander.kauffmann@kit.edu.

References

1. M. F. Yan, J. B. MacChesney, S. R. Nagel, W. W. Rhodes, Sintering of optical wave-guide glasses. Journal of Materials Science, 1980. 15(6): p. 1371-1378. DOI: 10.1007/BF00752116.

2. M. Meyer, M. Kramer, M. Akinc, Boron-doped molybdenum silicides. Advanced Materials, 1996. 8(1): p. 85-88. DOI: 10.1002/adma.19960080118.

3. M. K. Meyer, A. J. Thom, M. Akinc, Oxide scale formation and isothermal oxidation behavior of Mo–Si–B intermetallics at 600–1000°C. Intermetallics, 1999. 7(2): p. 153-162. DOI: 10.1016/S0966-9795(98)00058-2.

4. K. Yoshimi, S. Nakatani, T. Suda, S. Hanada, H. Habazaki, Oxidation behavior of Mo$_5$SiB$_2$-based alloy at elevated temperatures. Intermetallics, 2002. 10(5): p. 407-414. DOI: 10.1016/S0966-9795(02)00013-4.

5. Y. Yang, H. Bei, S. Chen, E. P. George, J. Tiley, Y. A. Chang, Effects of Ti, Zr, and Hf on the phase stability of Mo$_{SS}$+ Mo$_3$Si+ Mo$_5$SiB$_2$ alloys at 1600°C. Acta Materialia, 2010. 58(2): p. 541-548. DOI: 10.1016/j.actamat.2009.09.032.

6. A. Rahmel, P. J. Spencer, Thermodynamic Aspects of TiAl and TiSi$_2$ Oxidation: The Al-Ti-O and Si-Ti-O Phase Diagrams. Oxidation of Metals, 1991. 35(1-2): p. 53-68. DOI: 10.1007/BF00666500.

7. T. A. Parthasarathy, M. G. Mendiratta, D. M. Dimiduk, Oxidation mechanisms in Mo-reinforced Mo$_5$SiB$_2$ (T2)–Mo$_3$Si alloys. Acta Materialia, 2002. 50(7): p. 1857-1868. DOI: 10.1016/S1359-6454(02)00039-3.

8. S. Paswan, R. Mitra, S. K. Roy, Oxidation behaviour of the Mo–Si–B and Mo–Si–B–Al alloys in the temperature range of 700–1300°C. Intermetallics, 2007. 15(9): p. 1217-1227. DOI: 10.1016/j.intermet.2007.02.012.

9. D. Schliephake, A. Kauffmann, X. Cong, C. Gombola, M. A. Azim, B. Gorr, H.-J. Christ, M. Heilmaier, Constitution, oxidation and creep of eutectic and eutectoid Mo-Si-Ti alloys. Intermetallics, 2019. 104: p. 133-142. DOI: 10.1016/j.intermet.2018.10.028.

10. S. Obert, A. Kauffmann, M. Heilmaier, Characterisation of the oxidation and creep behaviour of novel Mo-Si-Ti alloys. Acta Materialia, 2020. 184: p. 132-142. DOI: 10.1016/j.actamat.2019.11.045.

507 11. S. Obert, A. Kauffmann, S. Seils, S. Schellert, M. Weber, B. Gorr, H.-J. Christ, M. Heilmaier,
508 On the chemical and microstructural requirements for the pesting-resistance of Mo-Si-Ti alloys.
509 JMR&T, 2020. 9(4): p. 8556-8567. DOI: 10.1016/j.jmrt.2020.06.002.

510 12. S. Majumdar, P. K. Singh, A. K. Pandey, G. V. S. N. Rao, Kinetics of oxide scale growth on a
511 $(Ti,Mo)_5Si_3$ based oxidation resistant Mo-Ti-Si alloy at 900-1300°C. High Temperature
512 Materials and Processes, 2019. 38(2019): p. 533-540. DOI: 10.1515/htmp-2019-0056.

513 13. M. A. Azim, B. Gorr, H.-J. Christ, O. Lenchuk, K. Albe, D. Schliephake, M. Heilmaier, Effect
514 of Ti content and nitrogen on the high-temperature oxidation behavior of $(Mo,Ti)_5Si_3$.
515 Intermetallics, 2017. 90: p. 103-112. DOI: 10.1016/j.intermet.2017.05.023.

516 14. J. Dai, J. Zhu, C. Chen, F. Weng, High temperature oxidation behavior and research status of
517 modifications on improving high temperature oxidation resistance of titanium alloys and
518 titanium aluminides: A review. Journal of Alloys and Compounds, 2016. 685: p. 784-798. DOI:
519 10.1016/j.jallcom.2016.06.212.

520 15. J. Unnam, R. N. Shenoy, R. K. Clark, Oxidation of commercial purity titanium. Oxidation of
521 Metals, 1986. 26(3-4): p. 231-252. DOI: 10.1007/BF00659186.

522 16. D. Vojtěch, B. Bártová, T. Kubatík, High temperature oxidation of titanium–silicon alloys.
523 Materials Science and Engineering: A, 2003. 361(1-2): p. 50-57. DOI: 10.1016/S0921-
524 5093(03)00564-1.

525 17. M. Yoshihara, Y.-W. Kim, Oxidation behavior of gamma alloys designed for high temperature
526 applications. Intermetallics, 2005. 13(9): p. 952-958. DOI: 10.1016/j.intermet.2004.12.007.

527 18. J. Angseryd, F. Liu, H.-O. Andrén, S. S. A. Gerstl, M. Thuvander, Quantitative APT analysis
528 of Ti(C, N). Ultramicroscopy, 2011. 111(6): p. 609-614. DOI: 10.1016/j.ultramic.2011.01.031.

529 19. R. Kirchhofer, D. R. Diercks, B. P. Gorman, J. F. Ihlefeld, P. G. Kotula, C. T. Shelton, G. L.
530 Brennecka, Quantifying Compositional Homogeneity in Pb(Zr, Ti)O_3 Using Atom Probe
531 Tomography. Journal of the American Ceramic Society, 2014. 97(9): p. 2677-2697. DOI:
532 10.1111/jace.13135.

533 20. F. Liu, K. Stiller, Atom probe tomography of thermally grown oxide scale on FeCrAl.
534 Ultramicroscopy, 2013. 132: p. 279-284. DOI: 10.1016/j.ultramic.2013.02.004.

535 21. F. Tang, B. Gault, S. P. Ringer, J. M. Cairney, Optimization of pulsed laser atom probe (PLAP)
536 for the analysis of nanocomposite Ti–Si–N films. Ultramicroscopy, 2010. 110(7): p. 836-843.
537 DOI: 10.1016/j.ultramic.2010.03.003.

538 22. T. Boll, M. Thuvander, S. Koch, J. N. Wagner, N. Nedfors, U. Jansson, K. Stiller, An APT
539 investigation of an amorphous Cr–B–C thin film. Ultramicroscopy, 2015. 159: p. 217-222. DOI:
540 10.1016/j.ultramic.2015.01.001.

541 23. J. I. Goldstein, S. K. Choi, F. J. J. V. Loo, G. F. Bastin, R. Metselaar, Solid-state Reactions and
542 Phase Relations in the Ti-Si-O System at 1373 K. Journal of the American Ceramic Society,
543 1995. 78(2): p. 313-322. DOI: 10.1111/j.1151-2916.1995.tb08802.x.

544 24. A. Abba, A. Galerie, M. Caillet, High-temperature oxidation of titanium silicide coatings on
545 titanium. Oxidation of Metals, 1982. 17(1-2): p. 43-54. DOI: 10.1007/BF00606192.

546 25. A. Escudero, F. Langenhorst, Incorporation of Si into TiO_2 phases at high pressure. American
547 Mineralogist, 2012. 97(4): p. 524-531. DOI: 10.2138/am.2012.3941.

548 26. S. Andersson, B. Collén, U. Kuylenstierna, A. Magnéli, Phase analysis studies on the titanium-
549 oxygen system. Acta Chemica Scandinavica, 1957. 11(10): p. 1641-1652.

550 27. P. G. Wahlbeck, P. W. Gilles, Reinvestigation of the Phase Diagram for the System Titanium–
551 Oxygen. Journal of the American Ceramic Society, 1966. 49(4): p. 180-183. DOI:
552 10.1111/j.1151-2916.1966.tb13229.x.

553 28. R. R. Merritt, B. G. Hyde, L. A. Bursill, D. K. Philp, The thermodynamics of the titanium +
554 oxygen system: An isothermal gravimetric study of the composition range Ti_3O_5 to TiO_2 at 1304
555 K. Philosophical Transactions of the Royal Society of London. Series A, Mathematical and
556 Physical Sciences, 1973. 274(1245): p. 627-661. DOI: 10.1098/rsta.1973.0078.

557 29. M. A. Azim, S. Burk, B. Gorr, H.-J. Christ, D. Schliephake, M. Heilmaier, R. Bornemann, P.
558 H. Bolívar, Effect of Ti (Macro-) Alloying on the High-Temperature Oxidation Behavior of
559 Ternary Mo–Si–B Alloys at 820–1300° C. Oxidation of Metals, 2013. 80(3-4): p. 231-242. DOI:
560 10.1007/s11085-013-9375-1.

561 30. D. A. Venkatu, L. E. Poteat, Diffusion of titanium of single crystal rutile. Materials Science and
562 Engineering, 1970. 5(5): p. 258-262. DOI: 10.1016/0025-5416(70)90014-5.

563 31. R. Beyers, Thermodynamic considerations in refractory metal-silicon-oxygen systems. Journal
564 of Applied Physics, 1984. 56(1): p. 147-152. DOI: 10.1063/1.333738.
565 32. G. B. Gibbs, Vacancy generation and the kinetics of oxidation. Philosophical Magazine, 1968.
566 18(156): p. 1175-1180. DOI: 10.1080/14786436808227748
567 33. Z. Liu, W. Gao, Y. He, Modeling of oxidation kinetics of Y-doped Fe–Cr–Al alloys. Oxidation
568 of Metals, 2000. 53(3-4): p. 341-350. DOI: 10.1023/A:1004545421739.
569 34. D. Naumenko, B. Gleeson, E. Wessel, L. Singheiser, W. J. Quadakkers, Correlation between
570 the microstructure, growth mechanism, and growth kinetics of alumina scales on a FeCrAlY
571 alloy. Metallurgical and Materials Transactions A, 2007. 38(12): p. 2974-2983. DOI:
572 10.1007/s11661-007-9342-z.
573 35. W. J. Quadakkers, Growth mechanisms of oxide scales on ODS alloys in the temperature range
574 1000–1100°C. Materials and Corrosion, 1990. 41(12): p. 659-668. DOI:
575 10.1002/maco.19900411204.
576 36. P. Kofstad, Oxidation of Metals: Determination of Activation Energies. Nature, 1957.
577 179(4574): p. 1362-1363. DOI: 10.1038/1791362a0.
578 37. C.-J. Han, C. R. Helms, Parallel oxidation mechanism for Si oxidation in dry O_2. Journal of The
579 Electrochemical Society, 1987. 134(5): p. 1297.
580 38. B. E. Deal, A. S. Grove, General Relationship for the Thermal Oxidation of Silicon. Journal of
581 Applied Physics, 1965. 36(12): p. 3770-3778. DOI: 10.1063/1.1713945.
582 39. M. Dechamps, P. Lehr, Sur l'oxydation du titane α en atmosphère d'oxygène: Rôle de la couche
583 oxydée et mécanisme d'oxydation. Journal of the Less Common Metals, 1977. 56(2): p. 193-
584 207. DOI: 10.1016/0022-5088(77)90041-8.
585 40. J. C. Mikkelsen, Self-diffusivity of network oxygen in vitreous SiO_2. Applied Physics Letters,
586 1984. 45(11): p. 1187-1189. DOI: 10.1063/1.95086.
587 41. D. K. Moore, D. J. Cherniak, E. B. Watson, Oxygen diffusion in rutile from 750 to 1000 degrees
588 C and 0.1 to 1000 MPa. American Mineralogist, 1998. 83(7-8): p. 700-711. DOI: 10.2138/am-
589 1998-7-803.
590 42. J. Rodríguez-Viejo, F. Sibieude, M. T. Clavaguera-Mora, C. Monty, [18]O diffusion through
591 amorphous SiO_2 and cristobalite. Applied Physics Letters, 1993. 63(14): p. 1906-1908. DOI:
592 10.1063/1.110644.
593 43. E. W. Sucov, Diffusion of Oxygen in Vitreous Silica. Journal of the American Ceramic Society,
594 1963. 46(1): p. 14-20. DOI: 10.1111/j.1151-2916.1963.tb13763.x.
595 44. T. Takahashi, S. Fukatsu, K. M. Itoh, M. Uematsu, A. Fujiwara, H. Kageshima, Y. Takahashi,
596 K. Shiraishi, Self-diffusion of Si in thermally grown SiO_2 under equilibrium conditions. Journal
597 of Applied Physics, 2003. 93(6): p. 3674-3676. DOI: 10.1063/1.1554487.
598 45. E. A. Gulbransen, K. F. Andrew, F. A. Brassart, Oxidation of Molybdenum 550° to 1700°C.
599 Journal of the Electrochemical Society, 1963. 110(9): p. 952-959. DOI: 10.1149/1.2425918.
600 46. E. S. Jones, J. F. Mosher, R. Speiser, J. W. Spretnak, The Oxidation of Molybdenum. Corrosion,
601 1958. 14(1): p. 20-26. DOI: 10.5006/0010-9312-14.1.20.
602 47. M. Simnad, A. Spilners, Kinetics and Mechanism of the Oxidation of Molybdenum. JOM, 1955.
603 7(9): p. 1011-1016. DOI: 10.1007/BF03377603.
604 48. R. W. Bartlett, Molybdenum Oxidation Kinetics at High Temperatures. Journal of The
605 Electrochemical Society, 1965. 112(7): p. 744-746.
606 49. T. Hatakeyama, S. Ida, N. Sekido, K. Yoshimi, Significant improvement of the oxidation
607 resistance of MoSiBTiC-based multiphase alloys by Ti enrichment. Corrosion Science, 2020:
608 p. 108937. DOI: 10.1016/j.corsci.2020.108937.
609 50. Z. Tang, J. J. Williams, A. J. Thom, M. Akinc, High temperature oxidation behavior of Ti_5Si_3-
610 based intermetallics. Intermetallics, 2008. 16(9): p. 1118-1124. DOI:
611 10.1016/j.intermet.2008.06.013.
612 51. J. He, R. K. Behera, M. W. Finnis, X. Li, E. C. Dickey, S. R. Phillpot, S. B. Sinnott, Prediction
613 of high-temperature point defect formation in TiO_2 from combined ab initio and thermodynamic
614 calculations. Acta Materialia, 2007. 55(13): p. 4325-4337. DOI:
615 10.1016/j.actamat.2007.04.005.
616 52. P. Kofstad, Note on the defect structure of rutile (TiO_2). Journal of the Less Common Metals,
617 1967. 13(6): p. 635-638. DOI: 10.1016/0022-5088(67)90111-7.

618   53.   P. Kofstad, Thermogravimetric studies of the defect structure of rutile (TiO_2). Journal of Physics
619   and Chemistry of Solids, 1962. 23(11): p. 1579-1586. DOI: 10.1016/0022-3697(62)90240-8.

620   54.   F. Millot, C. Picard, Oxygen self-diffusion in non-stoichiometric rutile TiO_{2-x} at high
621   temperature. Solid State Ionics, 1988. 28: p. 1344-1348. DOI: 10.1016/0167-2738(88)90384-0.

622   55.   P. Kofstad, P. B. Anderson, O. J. Krudtaa, Oxidation of titanium in the temperature range 800–
623   1200°C. Journal of the Less Common Metals, 1961. 3(2): p. 89-97. DOI: 10.1016/0022-
624   5088(61)90001-7.

625   56.   A. M. Chaze, C. Coddet, Influence of silicon on the oxidation of titanium between 550 and
626   700°C. Oxidation of metals, 1987. 27(1-2): p. 1-20. DOI: 10.1007/BF00656726.

627   57.   M. Yoshihara, K. Miura, Effects of Nb addition on oxidation behavior of TiAl. Intermetallics,
628   1995. 3(5): p. 357-363. DOI: 10.1016/0966-9795(95)94254-C.

629   58.   Z. Alam, D. K. Das, Effect of cracking in diffusion aluminide coatings on their cyclic oxidation
630   performance on Ti-based IMI-834 alloy. Corrosion Science, 2009. 51(6): p. 1405-1412. DOI:
631   10.1016/j.corsci.2009.03.027.

632   59.   A. Ashrafizadeh, F. Ashrafizadeh, Structural features and corrosion analysis of thermally
633   oxidized titanium. Journal of Alloys and Compounds, 2009. 480(2): p. 849-852. DOI:
634   10.1016/j.jallcom.2009.02.079.

635   60.   J. Stringer, Some observations on the kinetics of oxidation of titanium at high temperatures.
636   Journal of the Less Common Metals, 1964. 6(3): p. 207-213. DOI: 10.1016/0022-
637   5088(64)90100-6.

638   61.   P. Hidnert, Thermal expansion of titanium. J. Res. Natl. Bur. Stand, 1943. 30(1934): p. 101-
639   105.

640   62.   R. K. Kirby, Thermal expansion of rutile from 100 to 700 K. Journal of Research of the National
641   Bureau of Standards. Section A, Physics and Chemistry, 1967. 71(5): p. 363-369. DOI:
642   10.6028/jres.071A.041.

643   63.   I. Blech, U. Cohen, Effects of humidity on stress in thin silicon dioxide films. Journal of applied
644   physics, 1982. 53(6): p. 4202-4207. DOI: 10.1063/1.331244.

645   64.   P. F. Dennis, R. Freer, Oxygen self-diffusion in rutile under hydrothermal conditions. Journal
646   of Materials Science, 1993. 28(17): p. 4804-4810. DOI: 10.1007/BF00414275.

647